Advanced Functional Materials

ADVANCED FUNCTIONAL MATERIALS
www.afm-journal.de

RESEARCH ARTICLE

Landé *g*-factor Spectroscopy of Rydberg Excitons and Band Edge Electron-Hole Pairs in Two-Dimensional Hybrid Lead Halide Perovskite Films

Daniel Nikiforov[1] | Heshan Hewa Walpitage[1] | Binod Pandey[1] | Stephen McGil[2] | Dmitry Semenov[2] | Xiaomei Jiang[3] | Peter C. Sercel[4] | Zeev V. Vardeny[1]

[1]Department of Physics & Astronomy, University of Utah, Salt Lake City, Utah, USA | [2]National High Magnetic Field Laboratory, Tallahassee, Florida, USA | [3]Department of Physics, University of South Florida, Tampa, Florida, USA | [4]Center For Hybrid Organic Inorganic Semiconductors For Energy, Golden, Colorado, USA

Correspondence: Xiaomei Jiang (xjiang@usf.edu) | Peter C. Sercel (pcsercel@yahoo.com) | Zeev V. Vardeny (valy_vardeny@yahoo.com)

Received: 6 October 2025 | **Revised:** 5 March 2026 | **Accepted:** 9 March 2026

Keywords: electroabsorption | hybrid lead halide perovskites | Landé *g*-factor | magnetic circular dichroism | Rydberg excitons

ABSTRACT

We present a comprehensive investigation of the Landé *g*-factor of the exciton Rydberg series and band-edge electron-hole pairs in two-dimensional phenethylammonium lead iodide (PEPI) films using magnetic circular dichroism (MCD) spectroscopy. At low magnetic field ($B < 0.5$ T), we observe a sizable difference of 15%–20% between the effective *g*-factors of the 1s exciton and that of the higher energy Rydberg excitons, which overlap with the interband (IB) electron-hole (e-h) pair transitions at the band-edge (labeled here as the "2s+" band). At $T = 3$ K, we obtained $g_{1s} = 1.86 \pm 0.15$ and $g_{2s+} = 2.33 \pm 0.15$. These results demonstrate that the exciton *g*-factor is smaller than the sum of the individual electron and hole band edge *g*-factors, namely $g_{exciton} < g_e + g_h = g_{IB}$. The experimental results are rationalized by theoretical calculations of the *g*-factors using a multiband effective-mass model that includes the electron-hole interaction for the different exciton states. It is shown that with the decreasing spatial extent of the exciton wavefunction, the exciton *g*-factor also decreases. At $B > 10$ T, the interband Landau level transition (N = 1) extrapolates to the bandgap value in PEPI at $E_g = 2.62 \pm 0.016$ eV, providing further evidence of the formation of Rydberg excitons.

1 | Introduction

Phenethylammonium lead iodide (PEA_2PbI_4 or PEPI) is a widely studied two-dimensional (2D) Ruddlesden–Popper hybrid layered perovskite that possesses a natural multiple-quantum well structure consisting of alternating inorganic well and organic barrier layers [1]. The width of the inorganic $(PbI_6)^{4-}$ layer is ~0.64 nm, and the organic PEA layer is ~1 nm thick [2, 3]. PEPI crystallizes in the space group, $P\bar{1}$,(no. 2) [4] with the stacking direction along the c-axis (near normal to the layers) (see Figure S1.1a). The bandgap of PEPI has been commonly accepted to be ~2.57 eV [2, 5, 6], although a larger value of 2.625 eV was also reported [7]. Due to quantum and dielectric confinements, the excitons in PEPI play a crucial role in shaping its optical and electronic properties [7–12].

The energy structure of the excitons in various 2D layered hybrid perovskites, similar in structure to PEPI, has been reported to have a series of discrete levels following a 2D Wannier exciton model [13] (inset in Figure 4c). The lowest lying exciton ($n = 1$), namely the 1s exciton, is tightly bound and has a binding energy of a few hundreds of meV [5, 7, 14, 15]. The excitons in higher states ($n \geq 2$), commonly known as *Rydberg excitons*, are more loosely bound with a binding energy of up to a few tens of meV

[13, 14, 16–18]. As a result, the Rydberg excitons have extended spatial radii compared to those of the 1s exciton [14, 18], and may be more susceptible to applied perturbations such as an electric field.

The electron-hole (e-h) exchange interaction, combined with the crystal field and spin-orbit coupling (SOC), splits the 1s exciton level into four exciton fine structure (EFS) sub-levels. In PEPI, the lowest EFS state is the electric-dipole forbidden dark state (D exciton), followed by the two bright states, X and Y, having in-plane dipole orientation and capable of coupling to light incident normal to the layers. The highest EFS state has an out-of-plane dipole orientation (Z exciton) [19–22]. However, the energetic order of the Z exciton relative to that of X and Y may differ in various systems, as the energetic order is parameter dependent [21, 22].

XRD spectrum shows that the inorganic layers in PEPI are oriented parallel to the substrate plane, with an average crystal grain size of a few microns (Figure S1.1). This plane (labeled as the x-y plane) contains the primitive translation vectors $\boldsymbol{a}$ and $\boldsymbol{b}$, with primitive vector $\boldsymbol{c}$ oriented mainly out of plane (z-direction). Hence, for light propagating along the z-direction ($\vec{k} \parallel \hat{z}$), the optical absorption is mainly determined by the in-plane X and Y excitons [19, 22]. In particular, the X and Y excitons in PEPI have been shown experimentally to be split by zero-field splitting (ZFS) energy of ~2 meV [19, 21–24]. The relatively large ZFS could, in principle, complicate the interpretation of magneto-optical experiments in PEPI since it surpasses the Zeeman splitting up to relatively high magnetic fields of order ~10 T [23]. Below, we analyze in detail the impact of finite ZFS on the magnetic circular dichroism (MCD) spectrum.

In general, under the application of a magnetic field, the Zeeman interaction results in splitting of the electronic energy levels and changes in the oscillator strength of the optical transitions (see Section S3). The physical parameter that describes the Zeeman interaction of charge carriers (electrons or holes) with the magnetic field is the respective Landé g-factor, g_e and g_h. Our present study is focused on $g_{\parallel}$ (or g_z) measured in the Faraday configuration, with magnetic field normal to the sample plane, thus near parallel to the crystal c-axis.

MCD spectroscopy is a powerful tool used to obtain the Landé g-factor of electron-hole pairs and excitons [25]. We refer the readers to Section S1.2 for further details about the MCD method. For a given magnetic field orientation, the effective g-factor of an exciton, g_{EX}, depends on the individual electron and hole g-factors that contribute to the excitation. g_{EX} of the bright excitons X&Y in PEPI have been studied extensively, and their value has a widespread range from 1.2 to 2.3 [8, 19, 20, 23, 24, 26, 27].

Importantly, there is a fundamental question regarding the relation of g_{EX} to the electron and hole g-factors, which for the X&Y excitons in Faraday configuration is usually assumed to be $g_{EX} = g_e + g_h$ [22, 28]. This relation certainly describes the g-factor governing magnetic field splitting of transitions creating *uncorrelated* electron /hole pairs, i.e., in the case of the interband (IB) transition, $g_{IB} = g_e + g_h$. Yet, strong electron-hole (e-h) interaction exists in tightly bound excitons, and therefore, ignoring e-h interactions is unjustified. In fact, recent reports confirmed that g_{EX} in 2D PEPI is smaller than the sum of individually measured g_e and g_h [26]. Also, a recent theoretical study of the exciton g-factor in 2D transition metal dichalcogenides (TMDs) by Deilmann et al. [29] highlights the effect of many-body interactions in determining g_{EX}: It was demonstrated theoretically that g_{EX} is reduced by more than 30% from g_{IB} in $MoSe_2$ upon inclusion of electron-hole (e-h) interactions. PEPI shares many similarities with 2D-TMDs, such as large exciton binding energy and strong confinement [30, 31]. A more sophisticated theoretical model considering the e-h interactions and the extent of the exciton wavefunction in k-space is needed to account for the experimental observation that $g_{EX} < g_e + g_h$ [26].

Another thorny issue in PEPI photophysics is the value of its bandgap, E_g, which is usually obtained from the zero crossing of the electro-absorption (EA) response near the onset of a broad absorption band around 2.57 eV in majority of reports [5, 6, 8, 32]; while a few reports have stated a higher value of E_g [7, 17]. Since E_g is one of the fundamental parameters determining the optoelectronic properties of PEPI, this discrepancy should be further investigated.

In this work, we focus on the low-field (B < 0.5 T) MCD spectroscopy of PEPI films. In addition, we measured MCD spectra at high fields up to 30T. Importantly, we show theoretically that the MCD spectroscopy is *insensitive* to the ZFS in the limit of a wide optical transition spectral linewidth (LW). From the MCD spectra we obtained a sizable difference of 15%–20% for the Landé g-factors of the tightly bound 1s exciton and the Rydberg excitons (n≥2), which spectrally overlap with the IB edge electron-hole (e-h) pair transitions (labeled here as the "2s+" band). At temperature T = 3K, we obtained $g_{1s} = 1.86 \pm 0.15$, while $g_{2s+} = 2.33 \pm 0.15$. Our results are rationalized with a theoretical calculation based on the model of Deilmann et al. [29], implemented using a multiband effective mass theory description of the electron-hole interaction in excitons and incorporating a **K•P** description of the k-dependent electron and hole g-factors. Applying MCD at high magnetic field (B > 10T), we also observe the interband (IB) Landau level (N = 1) transition from which we evaluated the bandgap value of PEPI to be 2.619 ± 0.016 eV (at T = 16 K).

2 | Results and Discussion

2.1 | The Interplay Between Zeeman Splitting and ZFS in the MCD Spectroscopy

Figure 1a shows a schematic illustration of the MCD experimental set-up in the Faraday configuration, with the incident light wave vector parallel to the applied magnetic field ($\vec{k} \parallel \vec{B}$), with $\vec{B}$ perpendicular to the film's surface along the z-direction, i.e., $B = B_z$. Details of the experiment can be found in Section S1.3.

Figure 1c illustrates the case where X&Y excitons are degenerate (i.e., ZFS = 0), or near degenerate (i.e., at high magnetic field, where ZFS≪ $g\mu_b B_z$, hence ZFS can be reasonably approximated

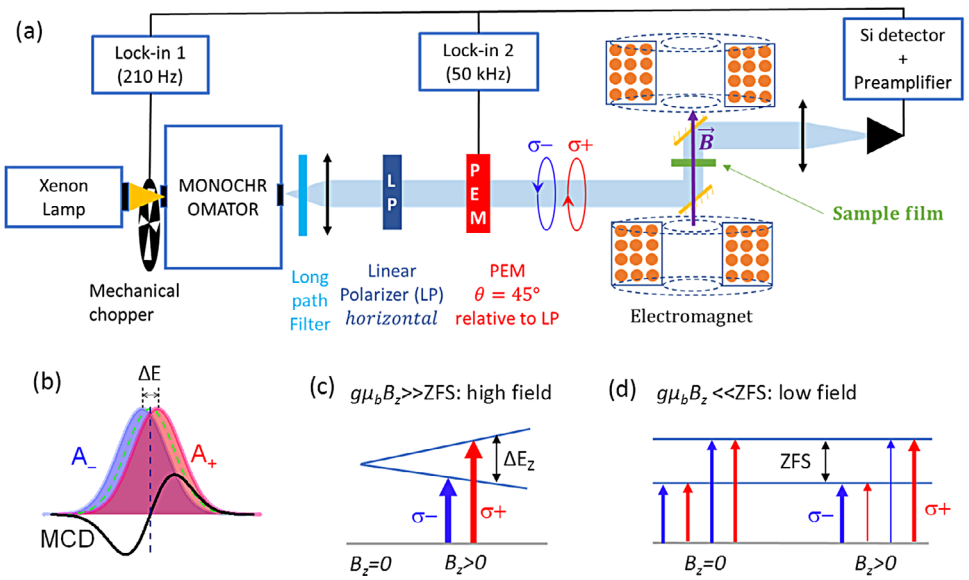

FIGURE 1 | Magnetic circular dichroism (MCD) schematic. (a) A schematic illustration of the low-field MCD experimental setup. The measurements are performed in the Faraday configuration ($\vec{k} \parallel \vec{B}$), with an external magnetic field applied perpendicular to the sample plane. We refer the reader to Section S1.3 for details. (b) Filled red (A+) and blue (A−) lines represent the absorbance bands that contribute to the absorption of left ($\sigma+$) and right ($\sigma-$) circularly polarized light, respectively. The black solid line shows the MCD spectrum (Equation 1). Panels (c) and (d) display schematically the origin of the MCD response in two limits: (c) high magnetic field limit: the zero field splitting (ZFS) is negligible in comparison to the magnetic energy ($\mu_B B \gg$ ZFS) and (d) low magnetic field limit: $\mu_B B \ll$ ZFS. The red (blue) arrows indicate electric dipole transitions for left, $\sigma+$ (right, $\sigma-$), circularly polarized light. The thickness of the arrows indicates the relative oscillator strength of the optical transitions.

as zero). In this case, with increasing magnetic field, the energy splitting, ΔE_z, between the two absorbance bands $A_\pm$ (Figure 1b) increases linearly with B_z, but the oscillator strength of the optical transition does not change with B_z. This is the ordinary Zeeman splitting case (Equation S3.4).

On the other hand, when X and Y excitons are *non-degenerate*, and ZFS cannot be ignored (Figure 1d), at low magnetic field, the energy splitting (ΔE_z) between the two absorbance bands $A_\pm$ nearly equals the ZFS, with a small quadratic correction term (Equation S3.19). In this case, it is primarily the intensity of the two bands $A_\pm$ that changes nearly linearly with increasing B_z (Equations S3.21–S3.23). We note that this interplay was nicely shown experimentally by Do et al. by measuring circularly and linearly polarized PL in a PEPI single crystal [24].

In Section S3, we show analytically that as long as the linewidth (LW) of the absorption bands is far greater than the ZFS and the magnetic energy (LW $\gg$ ZFS, $\mu_B B$), the experimental MCD response takes the form:

$$MCD = \Delta A = A_{L(\sigma+)} - A_{R(\sigma-)} = -\Delta E_{MCD} \frac{dA}{dE} \quad (1)$$

where,

$$\Delta E_{MCD} = g_{eff}\, \mu_B B \quad (2)$$

This calculation shows that the g-factor obtained from the MCD response is not affected by the consideration of non-zero ZFS, provided that the linewidth is large.

2.2 | The MCD Spectra at Low Magnetic Field: Extraction of the Landé g-factors

Figure 2a presents the zero-field absorption spectrum of a PEPI thin film measured at T = 3 K. Three well-resolved bands equally separated by about 40 meV are due to the 1s exciton at 2.349 eV and its respective phonon replicas, 1s+1 ph, and 1s+2 ph. The fit using a Frank-Condon formalism (Equation 3) confirms the vibronic progression [33], with a Huang Rhys parameter S = 0.25 and phonon energy $h\nu$ = 41 meV. The phonon energy matches well with the rotational mode of the organic cations [34]. Table 1 lists details of these excitonic bands.

$$\alpha\ (E) = \alpha_0 + a \sum_{n=0}^{2} \frac{e^{-s} s^n}{n!} f\ (E, n, w) \quad (3)$$

where $f\ (E, n, w) = \frac{2}{\pi} \frac{w}{4(E - E_0 - nh\nu)^2 + w^2}$ is a lineshape function, taken to be Lorentzian for the transitions involved. In this expression, the broadening parameter w is the line width (LW) defined as the full-width at half maximum (FWHM), whereas the parameter a is proportional to the oscillator strength of the 1s exciton. The parameter α_0 reflects non-resonant background scattering/absorption.

Figure 2b presents MCD spectra of the PEPI thin film at 3 K, measured at two field polarities of $B_z = \pm$ 0.42 T. The spectral shape closely follows the first derivative of the absorption spectrum (Figure 2a), with three pronounced zero-crossings that correspond to the 1s exciton and its two phonon replicas. The MCD spectrum for each field value can be well fit (black solid lines), using Equation (1) and the experimental absorption

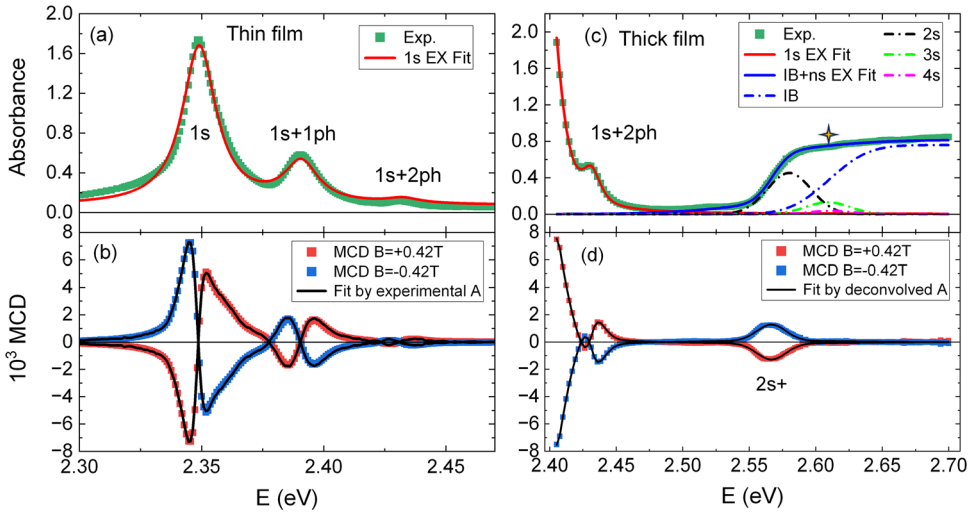

FIGURE 2 | The absorption and MCD spectra of two PEPI films measured at $T = 3$ K: The spectra collected in thin, 30 ± 5 nm, (a, b) and thick, 365 ± 20 nm, (c, d) films are presented. The MCD spectra at $B_z = \pm 0.42$ Tesla are represented by red/blue squares as indicated in the legends of (b, d). The red line in (a) is a fit of the thin film absorption spectrum that includes the 1s exciton and its vibrational overtones using Equation (3). The fit of the absorption spectrum in the thick film (c) is done by deconvolving the absorbance of the exciton (red line, c) and the overlapping Rydberg excitons and interband (blue line, c) absorbance bands. The broken lines are the individual transitions from the Rydberg excitons (2s, 3s, ns ($n \geq 4$)), and interband (IB). The star in (c) marks the bandgap, E_g.

TABLE 1 | Transition energies, linewidths, and spectral weights of the exciton lines in PEPI. Equation (3) is used to fit the tightly bound 1s exciton and its phonon replicas (Figure 2a), whereas Equation (4) is used for the more loosely bound Rydberg excitons and IB transition (Figure 2c). For the 1s exciton, the FWHM LW equals the fitted Lorentzian broadening parameter w from Equation (3). For the Rydberg excitons and IB transition, the FWHM LW is related to the corresponding fitted broadening parameters by $LW_{EX} = 2\sqrt{2\ln 2}\,\sigma_{EX}$ or $LW_{IB} = 2\sqrt{2\ln 2}\,\sigma_{IB}$. The spectral weights are calculated separately for the 1s exciton and its phonon replicas, and for the Rydberg excitons and IB transition.

	1s	1s+1ph	1s+2ph	2s	3s	ns ($n \geq 4$)	IB edge (E_g)
Energy (eV)	2.3495	2.3906	2.4297	2.580	2.609	2.612	2.610
FWHM LW (meV)	17	17	17	39	39	39	58
Spectral weight	78%	20%	2%	63%	10%	2%	25%

spectrum, with a single fitting parameter, namely ΔE_{MCD}. Figure S1.4 demonstrates zoomed-in regions of the MCD fitting; it is seen that a good fit is obtained for all three exciton-related absorption bands (namely 1s and 1s+phs). We obtained $g_{1s} = 1.86 \pm 0.15$ using a linear fit of $\Delta E_{MCD}(B)$, Equation (2), see Figure 3b (black squares). The single g-factor confirms that the three absorption bands are indeed related to each other via phonon progression. See Section S1.3.2 for details of the fitting procedure.

According to the Elliott model [35], the large binding energy of the 1s exciton in PEPI results in a weak IB transition strength, as seen in this thin film (see also Figure S1.6). Furthermore, the 2D Wanier exciton model predicts a fast drop-off of the oscillator strength for the Rydberg excitons with n > 2 [14]. Therefore, to investigate the MCD spectra of the Rydberg excitons and the IB transition, we conducted MCD measurements on a thick PEPI film (thickness of 365 ± 20 nm). As seen in Figure 2c, the tail of the 1s exciton absorption that contains 1s+2 ph band is still present (1s and 1s+1ph peaks are not shown due to saturation) together with a step-like absorption band from the combined Rydberg excitons and IB edge transition. The common practice is to take the zero crossing in the EA spectrum near the onset of this step-like absorption as the bandgap E_g [5, 6]. However, the spectrally crowded region, including Rydberg excitons and their respective phonon replicas, can produce a 'ramp' below the actual IB transition energy. To demonstrate this effect, we show in Figure 2c the fit of the step-like absorption by the sum of absorption from 2s, 3s, and ns ($n \geq 4$) excitons (black, green, and magenta broken lines) weighted by their respective oscillator strength [14], combined with the 2D type IB edge absorption (blue broken line) using the following equation:

$$\alpha\ (E) = \alpha_0 + \alpha_{EX} \sum_{i=2}^{n} f_i \frac{e^{-\frac{(E-E_i)^2}{2\,\sigma_{EX}^2}}}{\sigma_{EX}\sqrt{2\pi}} + \alpha_{IB}\left(\frac{1 + \mathrm{erf}\left(\frac{E-E_g}{\sqrt{2}\,\sigma_{IB}}\right)}{2}\right) \quad (4)$$

Here, f_i is the oscillator strength of the i^{th} (i = 2,3,4&up) Rydberg exciton [14], with E_i the respective transition energy. The term σ_{EX} denotes the transition broadening parameter for the Rydberg excitons, within a Gaussian lineshape function. This is related to the transition linewidth (LW), defined as the full width at half maximum (FWHM), by $LW_{EX} = 2\sqrt{2\ln 2}\,\sigma_{EX} \cong 2.355\,\sigma_{EX}$, taken to be identical for all Rydberg exciton transitions. For the IB edge

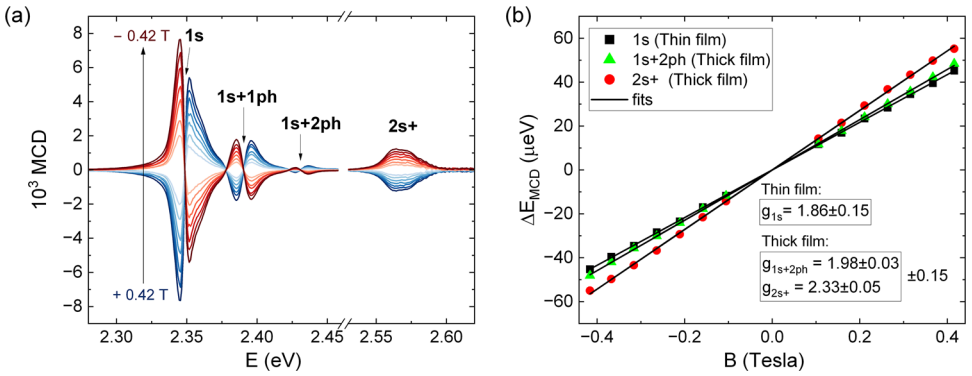

FIGURE 3 | MCD and *g*-factor determination. (a) MCD spectra of thin and thick PEPI films (separated by a gap) measured at T = 3 K, under magnetic field, *B*, ranging from +0.42 T to − 0.42 T. (b) The MCD shift, ΔE_{MCD}, vs the field B_z, from which the Landé *g*-factors of the 1s (black squares), 1s+2 ph (green triangles), and 2s+ (red circles) excitons are extracted using Equation (1) and (2). The larger error of ± 0.15 must be considered when comparing *g*-factor values between different films. However, when comparing the *g*-factor values associated with different spectral features determined within the same experiment (here, the thick film), the smaller error can be considered.

absorption term, α_{IB} denotes the magnitude of the absorption above the band gap, E_g, while σ_{IB} denotes the broadening parameter for the individual interband free carrier absorption transitions that, when summed, produce the broadened step-function seen in the last term on the right side of Equation (4). The parameter σ_{IB} is related to the FWHM of the individual IB free carrier absorption transitions by $LW_{IB} = 2\sqrt{2\ln 2}\,\sigma_{IB} \cong 2.355\,\sigma_{IB}$. LW_{IB} is also the linewidth of the Gaussian that results from taking the derivative of the total IB absorption (last term on the right side of Equation (4)—this derivative is proportional to the corresponding interband transition MCD response. From the fitting, the bandgap was extracted to be $E_g = 2.61 \pm 0.02$ eV (indicated by the star in Figure 2c).

To evaluate the relative contributions from the Rydberg excitons and IB transition, the integrated intensity of each band up to E_g (star in Figure 2c) was calculated (see details in Table 1). The dominance of Rydberg excitons over IB is clear: The sum of the spectral weights of the Rydberg excitons is over 75%. Among the Rydberg excitons, the 2s exciton has the highest contribution (63% of the total spectral weight). Hence, the absorption edge (aka, the ramp) is mostly determined by the Rydberg excitons, rather than the IB transition. We thus label this absorption ramp as 2s+ to highlight the main contribution from the 2s exciton, but other Rydberg excitons and IB e-h pairs also contribute. We note that 2s+ is a band label, not a state label.

Figure 2d displays the MCD spectra of the thick film at 3 K, measured at two polarities of $B_z = \pm 0.42$ T. As seen, the spectral shape closely follows the first derivative of the absorption spectrum, with the zero-crossing at 2.430 eV for the 1s+2 ph transition, and a broad band at 2.57 eV for the 2s+ transition. We fit the MCD spectra using Equations (1) and (2), similar to what is done in the thin film for the 1s exciton (Figure 2b). However, the complete MCD spectra cannot be fit with a single *g*-factor. The best fit is obtained using two *g*-factors, namely $g_{1s+2ph} = 1.98 \pm 0.03$ for the 1s+2 ph band, and $g_{2s+} = 2.33 \pm 0.05$ for 2s+ band.

Figure 3a shows MCD spectra in the full spectral range at various magnetic field strengths at 3 K. In Figure 3b, we plot the magnetic field dependence of the extracted ΔE_{MCD} value from Equation (1), for the 1s (black squares), 1s+2 ph (green triangles), and 2s+ (red circles) excitons. All three energy shifts exhibit a linear dependence on B_z, consistent with Equation (2). The extracted *g*-factor values of the three photoexcitations are listed in Figure 3b. The difference between the *g*-factors of the 1s exciton measured for the thin and thick (g_{1s+2ph}) films is within the experimental uncertainties among different measurements as explained in Section S1.3.2. Importantly, the higher precision of the *g*-factors can be used for calculating the difference between the *g*-factor values obtained in the same experiment, as indicated in Figure 3b caption. We therefore conclude that the difference between g_{2s+} and g_{1s+2ph}, which is more than 15%, is intrinsic, rather than due to experimental error and/or sample variation. Hence, our results demonstrate that the 1s, Rydberg excitons, and IB e-h pairs all have different effective *g*-factor values.

To explain this result, we refer to the theoretical analysis of the relation between the exciton *g*-factor (g_{EX}) and the IB e-h pair *g*-factor (g_{IB}) in TMD systems advanced by Deilmann et al. [29]. These authors found theoretically that g_{EX} is reduced by more than 30% from g_{IB} in $MoSe_2$ upon inclusion of electron-hole (e/h) interactions. We adapt the model given in Ref. [29] to the selection rules for Faraday geometry in the perovskite PEPI for a magnetic field applied along *z*. In this case, the *g*-factor, $g^z_{n,0}$, for an optically active Wannier-type 2D exciton state with principal quantum number *n* and azimuthal quantum number $m = 0$, can be expressed as:

$$g^z_{n,0} = \int \left|\tilde{\phi}_{n0}(\boldsymbol{k})\right|^2 \left(g^z_e(\boldsymbol{k}) + g^z_h(\boldsymbol{k})\right) \mathrm{d}^2k \qquad (5)$$

The integrand here comprises the sum of the $\boldsymbol{k}$-dependent electron and hole *g*-factors, weighted by the norm-square of the $\boldsymbol{k}$-space representation of the relative wave function extent of the 2D exciton, denoted as $\tilde{\phi}_{n0}(\boldsymbol{k})$. For comparison, the corresponding expression for the *g*-factor governing the Zeeman splitting of the band edge transition, g^z_{IB}, is the sum of the electron and hole *g*-factors at $\boldsymbol{k} = 0$:

$$g^z_{IB} = g^z_e + g^z_h \qquad (6)$$

which is the usual result for transitions producing uncorrelated electron-hole pairs by magneto-absorption in the Faraday arrangement, given the optical selection rules in PEPI (Section S2.3).

To apply Equation (5) in PEPI, we use expressions for the $\boldsymbol{k}$-space representations of the exciton wave functions given in Section S2 in Table S2-3, parameterized by the calculated exciton parameters (binding energy, radius) summarized in Table S2-2 within Section S2.1. The calculations reflected in Table S2-2 are performed variationally using the trial 2D exciton relative wave functions given in Table S2-1, employing Guseinov's exact solution for the electron-hole interaction for an electron and a hole embedded in a dielectric superlattice [36] using the material parameters given in panel (a) of Table S2-2. The variational procedure itself is outlined in detail within the SI of Steger et al., Ref. [37]. We use the Guseinov potential in favor of simpler three-layer slab dielectric models introduced by Rytova [38] and Keldysh [39] or the commonly employed three-layer slab image charge potential introduced by Hanamura [40], as these three-layer slab dielectric models are known to be inaccurate in systems where the low dielectric layer thickness is comparable to the high dielectric well thickness, such as in PEPI [37]. The exciton g-factor calculation also requires the k-dependent electron and hole g-factors as inputs. Analytical expressions for these are derived using the theory of Roth et al. [41], generalized [42] to address states of non-zero wave-vector $\boldsymbol{k}$; this calculation is based on an 8-band **K.P** model for the conduction and valence bands (described in Section S2.3.2). Neglecting anisotropy in the plane of the inorganic layer, the hole g-factor, $g_h^z(\boldsymbol{k})$, with $\boldsymbol{k}$ in the k_x,k_y plane, is:

$$g_h^z(\boldsymbol{k}) = g_0 - E_p\left(\frac{\cos^2\theta}{E_c(\boldsymbol{k}) - E_v(\boldsymbol{k})} + \frac{\sin^2\theta}{E_{le}(\boldsymbol{k}) - E_v(\boldsymbol{k})} - \frac{1}{E_{he}(\boldsymbol{k}) - E_v(\boldsymbol{k})}\right) + \delta g_h \quad (7)$$

Here $g_0 = |g_e|$ is the free electron spin g-factor, approximately equal to 2.0023; E_p is the Kane energy [43]; while $E_v(\boldsymbol{k})$, $E_c(\boldsymbol{k})$, $E_{he}(\boldsymbol{k})$, and $E_{le}(\boldsymbol{k})$ are energies of the valence band, the conduction band, and the heavy- and light-electron band at a given $\boldsymbol{k}$ in the k_x,k_y plane (see Sections S2.2.1 and S2.3.2). In the above expression, the phase angle θ, given in Equation S2.14, depends on the spin-orbit split-off parameter, Δ, which separates the $J = 1/2$ lowest conduction band from the $J = 3/2$ heavy- and light-electron bands at $k = 0$, and the tetragonal crystal field δ, which reflects the asymmetry between the in-plane and out-of-plane directions in 2D perovskites such as PEPI [44]. Finally, δg_h is a correction due to remote band coupling. This term is introduced following the analysis of Ref. [45], where a discrepancy between the 8-band **K•P** model for the hole g-factor was found in quantum confined nanocrystals, which was suggested to be due to coupling of the highest valence band with lower remote valence bands. The corresponding result for the electron g-factor, $g_e^z(\boldsymbol{k})$, is:

$$g_e^z(\boldsymbol{k}) = g_0\left(\sin^2\theta - \cos^2\theta\right) + \cos^2\theta\frac{E_p}{E_c(\boldsymbol{k}) - E_v(\boldsymbol{k})} + \delta g_e + \cos^2\theta\frac{1}{E_c(\boldsymbol{k}) - E_{he}(\boldsymbol{k})}\left(144\,\gamma_2\gamma_3\frac{\hbar^2}{m_0}k^2\right) \quad (8)$$

Here, the term δg_e represents remote band contributions to the electron g-factor following Ref. [45, 46] where this correction was assigned predominantly to conduction band coupling to remote (lower) valence bands outside the 8-band model. The last term, which reflects coupling between the $J = 1/2$ and $J = 3/2$ conduction bands, depends on the product of the Luttinger effective parameters γ_2, γ_3 which are related to the heavy- and light- electron band effective masses (see Section S2.3 for more details).

To evaluate Equation (5) for the exciton g-factors here, we employ material parameters of PEPI summarized in the Table S2-4 as follows: The fundamental gap is estimated here on the basis of the high magnetic field measurements described below; the spin-orbit split-off parameter, the crystal field, and the Kane energy are taken from Ref. [37]; while the band edge effective mass is taken as the experimental value reported in Ref. [7]. We assume the light and heavy electron masses to be the same as those of the lowest conduction band. To estimate the remote band contribution to the hole g-factor, δg_h, we constrain the calculated band edge hole g-factor to match the experimental value $g_{h,0}^z = -0.13$ reported in Ref. [26]. The remote band contribution to the electron g-factor, δg_e, is determined by requiring that either the g-factor of the band edge free-carrier transition (Equation 6), g_{IB}^z, or the g-factor of the 2s exciton, g_{20}^Z (Equation 5), matches the experimental value $g_{2s+}^z = 2.33$ determined above. The rationale for this dual approach to parameterization, which gives a range for the parameters as listed in Table S2-4, is based on the fact that we could not measure the g-factors of individual Rydberg exciton and IB carrier due to the spectral overlap, with the measured g_{2s+} being an overall g-factor comprising an average among the Rydberg excitons and band edge e-h pairs. Finally, the geometric mean, $\sqrt{\gamma_2\gamma_3}$, of the Luttinger parameters γ_2, γ_3 is determined by requiring that the g-factor of the $n = 1$, $m = 0$ exciton match experimental value measured in this work, $g_{1,0}^z = 1.86$, which has a higher fidelity. The fitted value, $\sqrt{\gamma_2\gamma_3} \cong 0.34 \sim 0.39$, is comparable to the value for $\gamma_2 \sim 0.25$ estimated within a 6 band **K•P** model in Ref. [37].

Figure 4a plots the calculated g-factors for Rydberg excitons and the IB e-h pair (values are shown in Table S2-5). As can be seen, the biggest difference is between g_{10} (1.86) and g_{20} (2.21), at about 16%; the difference between g_{20} and g_{IB} is only about 5%. These values match the experimental results quite well, as shown in Figure 4. We note in passing that it is impossible to assign g_{2s+} to g_{20} or g_{IB} with certainty. However, the essential point is that g_{1s} for tightly bound 1s exciton is considerably smaller than g_{2s+} for Rydberg excitons and IB carriers (loosely bound e-h pairs). Our work shows that the g-factors of excitons in PEPI are different for the various exciton Rydberg states and distinct from the value associated with the IB e-h pairs.

Figure 4b,c displays the calculated root-mean-square (rms) exciton wave function extent $\rho_{n,0}^{rms}$ and exciton binding energy ($E_{n,b}$), respectively, for $n = 1$–4 (values are in Table S2-2). Our calculation of $E_{n,b}$ matches well with the experimental results in this work and another report [17]. It is seen that the wavefunction extent of Rydberg excitons in real space is substantially larger than that of the 1s exciton. This explains why $g_{ns} > g_{1s}$. Our result is similar to what was reported in TMD [29, 47].

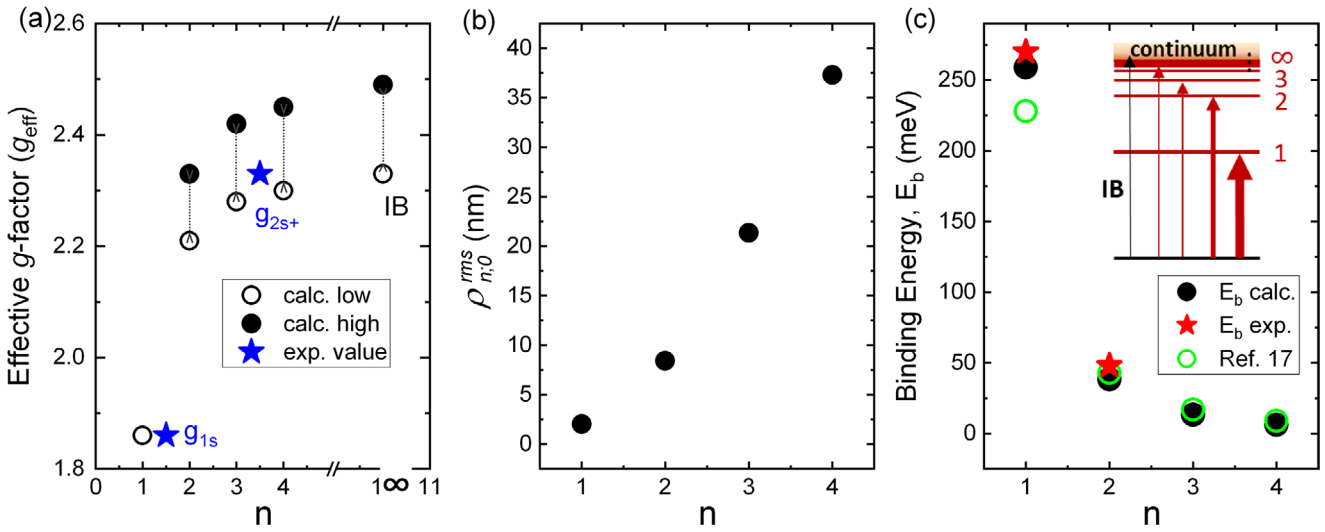

FIGURE 4 | Results of model calculation for the exciton g-factor, radius, and binding energies. (a) Effective g-factor of each exciton in the Rydberg series and the g-factor of the interband (IB) e-h pair. Both the lowest (black open circles) and the highest (black filled circles) calculated values are shown. (b) The calculated root-mean-square (rms) wave function extent $\rho^{rms}_{n,0} \equiv \sqrt{\langle \rho^2 \rangle_{n0}}$ is shown (black circles). (c) The calculated (black filled circles) and experimental (red stars) exciton binding energies (E_b) in the Rydberg series. See Table S2-5 for the values. Previously reported values of E_b for PEPI [17] are displayed (green open circles) alongside the present work values. The inset illustrates schematically the transitions between the ground state and the Rydberg states, which eventually merge with the continuum band.

2.3 | The MCD Spectra at High Magnetic Field: Extraction of the Bandgap (E_g) and Diamagnetic Shift Coefficient (C_{2s+})

Here, we discuss the MCD spectra measured at high magnetic fields in a thick PEPI film. Figure 5a presents several MCD spectra in the spectral range 2.53–2.70 eV. A prominent broad band (2s+ band) is seen centered at ~2.576 eV, similar to that in Figure 2d. It blueshifts quadratically with B_z at high magnetic field, due to the diamagnetic shift given in Equation (9) [48].

$$E_{2s+}(B) = E_{2s+}(0) + C_{2s+}B^2 \tag{9}$$

where C_{2s+} is the 'effective' diamagnetic coefficient of the 2s+ band. A good fit is seen in the inset of Figure 5a, from which we obtained $E_{2s+}(0) = 2.576$ eV, and $C_{2s+} = 7.25$ μeV/T. We do not observe a measurable diamagnetic shift for the 1s exciton within our experimental ability. However, the diamagnetic shift was measured to be less than 2 meV at $B_z > 60$ T [7]. Therefore, taking $C_{1s} = 0.36$ μeV/T [7], it is seen that $C_{2s+} \gg C_{1s}$, meaning the root-mean-square (rms) wave function extent of 2s+ band is much larger than that of the 1s exciton (as shown in Figure 4b), consistent with $g_{2s+} > g_{1s}$.

As the magnetic field increases, we observe the evolution of a broad band at energies above 2.60 eV. A magnified view of this feature is presented in Figure 5b (for $B_z < 0$) & Figure S1.8 (for $B_z > 0$). We assign this band due to the interband transition between Landau Levels (LL) in the valence band (VB) and conduction band (CB) that are induced by the high magnetic field [7, 49, 50]. Since the MCD spectra are proportional to the first derivative of the absorption spectrum, the LL transition photon energy can be extracted from the zero-crossing (marked as circles in Figure 5b).

The photon energy of the LL interband transitions from VB to CB without spin-orbit coupling may be expressed as:

$$E_N(B_z) = E_g + \left(N + \frac{1}{2}\right)\hbar\omega_c, \tag{10}$$

where N is the LL quantum number, and $\omega_c = \frac{eB}{\mu}$ is the effective cyclotron frequency of the combined electron and hole, using the reduced mass $\mu^{-1} = m_e^{-1} + m_h^{-1}$. This follows since optically allowed transitions only occur between the VB and CB states with the same N, with the lowest transition (N = 0) differing from the bandgap, E_g, by $\frac{1}{2}\hbar\omega_c$. However, due to the broadening of the IB onset (see Figure 2c), the (0,0) LL transition is not resolved in PEPI; actually, this transition has not been identified in magnetic fields as high as 65 T in reports elsewhere [7]. In our range of B_z (<30T), we believe that the observed transition is the N = 1 LL transition (LL(1,1)). A fit using Equation (10) yields $\mu = 0.11 \pm 0.06\, m_e$ and $E_g = 2.619 \pm 0.016$ eV. The values recently reported for PEPI crystals are within the experimental error of our result [7, 50]. The fact that the E_g value determined by LL spectroscopy is well above that determined by the EA spectrum (2.62 eV vs. 2.57 eV) strongly supports the hypothesis of the Rydberg exciton formation just below the energy gap, as demonstrated in Figure 2c. Our results echo an earlier statement by Plochocka et al. about the underestimated value of E_g in PEPI [7]. From our various measurements, we extract the binding energy of 1s and 2s excitons to be $E_{b,1s}$ = 2619−2349 meV = 270 ± 16 meV, and $E_{b,2s}$ = 2619−2571 meV = 48 ± 16 meV, respectively. Both values match well with the model calculation (Figure 4c, red stars) and are consistent with earlier reports [7, 12, 15]. Furthermore, $E_{b,2s+}/E_{b,1s} \approx 1/6$ as predicted in Ref. [16].

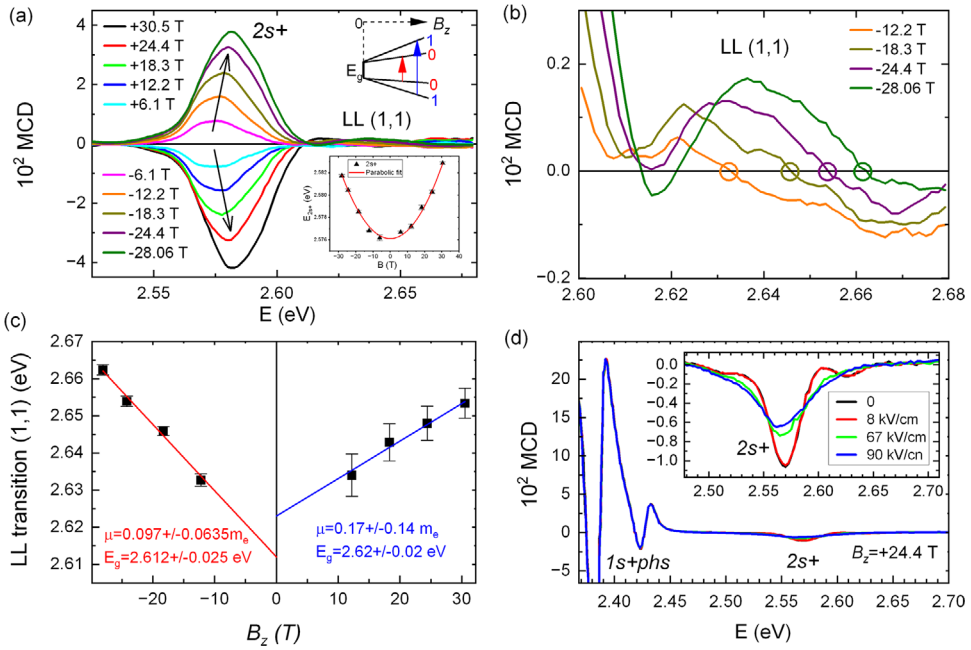

FIGURE 5 | MCD spectra at high magnetic field measured at $T = 16$ K. (a) The MCD spectra measured at field up to 30T show the 2s+ band and the interband N = 1 Landau level (LL) transition (labelled LL (1,1)). The lower inset shows the "2s+" band energy vs. B_z from which the diamagnetic shift coefficient C_{2s+} is obtained. The upper inset is a schematic drawing of the LL interband transitions. (b) Magnified view of the LL(1,1) transition with $B_z < 0$, where the circles indicate the transition energy at each magnetic field value. (c) LL(1,1) transition energy as a function of B_z from which the values of the exciton effective mass (μ) and bandgap E_g are obtained. The weighted average values are $\mu = 0.11 \pm 0.06\ m_e$ and $E_g = 2.619 \pm 0.016$ eV. (d) The MCD spectra at various applied in-pane electric field strengths (F), measured at $B_z = 24.4$ T. The inset shows a magnified view of the MCD spectrum of the 2s+ band.

Figure 5d demonstrates the dependence of the MCD spectra at $B_z = 24.4$ T measured under an in-plane applied electric field, F, up to 90 kV/cm. The electro-absorption (EA) setup is explained in Section S1.5. As seen, the MCD spectrum of the 1s exciton and its phonon replicas are robust to the electric field. By contrast, the MCD spectrum of 2s+ band is weakened and broadened by the electric field, with the LL (N = 1) transition at energies E > 2.63 eV being quenched completely at $F > 67$ kV/cm (inset of Figure 5d). This can be explained by the difference in the binding energies of the 1s and Rydberg excitons. Rydberg excitons are less strongly bound than the 1s exciton (as seen in Figure 4c) and are therefore expected to be partially ionized by the applied electric field [13]. As a result, the MCD of the 2s+ band is weakened and broadened with F. Note that the broadening of the 2s+ MCD band is asymmetric, with the higher n Rydberg excitons being affected more by the electric field (see the inset of Figure 5d). In addition, the electric field interferes with the formation of LL for the free carriers, hence the disappearance of the LL (1,1) feature from the MCD spectrum at applied voltage higher than 67 kV/cm [51].

3 | Conclusions

By implementing the low-field MCD spectroscopy ($B < 0.5$T), we demonstrate that the g-factor of the X,Y bright 1s exciton is smaller by 15%–20% compared to the sum of the individual electron and hole band edge g-factors, $g^{\parallel}_{1s;\,X,Y} < g^{\parallel}_e + g^{\parallel}_h = g^{\parallel}_{IB}$ ($\hat{c} \parallel \vec{B} \parallel \hat{z}$). This result implies that one cannot simply derive the values of the *uncorrelated* electron and hole g-factors by measuring the different exciton g-factors and using the relations which consider only the electron and hole band edge g-factors, for example: $g_{X,Y} \neq g_e + g_h$ and $g_D \neq g_e - g_h$. By implementing a multiband effective-mass model, we derive the $\vec{k}$-dependent $g^{\parallel}_h(\vec{k})$ and $g^{\parallel}_e(\vec{k})$ expressions (Equations 7 and 8, respectively). Accounting for the exciton wavefunction extent in $\vec{k}$-space, we are able to estimate the exciton g-factors (Equation 5). Following from this analysis, the smaller exciton wavefunction extent in real-space results in a reduced exciton effective g-factor. Hence, the exciton g-factor correlates with the exciton's radius. It is important to clarify that since the g-factors depend on many material parameters (Equations 7 and 8), a comparison of the g-factors alone between different materials does not permit direct conclusions about excitons' relative size. However, it is possible to estimate relative exciton sizes when comparing the g-factors of Rydberg excitons measured in the same system, as is demonstrated in the current work. We also show that the g-factor of bright excitons can be obtained in a low-field MCD setup (B < 0.5 T). On the other hand, obtaining information about the exciton radii in 2D materials from the diamagnetic shift requires high-field experiments (B >10 T). A possible implementation of our findings is the dependence of the g-factors on various environmental parameters (e.g. temperature, pressure). Lastly, our high-field MCD LL spectroscopy shows that in PEPI the absorption onset of the step-like absorption band originates from Rydberg excitons (mainly 2s) crowded just below the IB transition, whereby the true energy gap is at higher energy, namely $E_g = 2.62 \pm 0.016$ eV, in agreement with previous high-field studies [7, 50].

4 | Methods/Measurements

4.1 | Synthesis and Film Preparation

All solutions and sample preparations were carried out in a nitrogen-filled glove box. To prepare the precursor solution, 0.8 mmol of phenethylammonium iodide (805904, Sigma–Aldrich) and 0.4 mmol of lead(II) iodide (211168, Sigma–Aldrich) were dissolved in 2 mL of *N,N*-dimethylformamide (DMF; D119, Fisher Chemical), yielding a 0.2 M solution. The mixture was stirred overnight at room temperature. A portion of this stock solution was then diluted to obtain a 0.085 M solution.

For thin films (30 ± 5 nm, measured by AFM), the 0.085 M solution was spin-coated at 5000 rpm for 60 s. For thick films (365 ± 20 nm), the 0.2 M solution was spin-coated at 2000 rpm for 60 s. In both cases, the films were subsequently annealed on a hot plate at 100°C for 30 min.

4.2 | Magnetic Circular Dichroism (MCD) Spectroscopy

4.2.1 | Low-Field Setup

A home-made setup was used to measure the film transmission (T) and the change of T under a magnetic field $B < 0.5$T generated by a water-cooled resistive magnet. The experimental setup, measurement protocol, and data analysis are explained in detail in Section S1.3.

4.2.2 | High-Field Setup

Qualitatively, the setup was very similar to the one described above for the low-field experiment, but with different models for some of the equipment (Newport Cornerstone 260; PEM-100). The sample was placed in a liquid helium-cooled cryostat, and the magnetic field was provided by a resistive split magnet up to ∼ 30 T (National High Magnetic Field Laboratory, Cell #5). A broadband optical fiber was used to collect the light after passing through the sample.

4.3 | Electroabsorption (EA) Spectroscopy

The EA experiment in the current study was combined with MCD spectroscopy. The effect of a strong electric field, applied in the plane of the PEPI film, on the MCD spectra was demonstrated. Experimental details are summarized in Section S1.5.

Author Contributions

D.N. prepared the PEPI films, conducted the low-field MCD experiments (including realization of the low-field setup and data analysis). H.H. and B.P. fabricated the devices used in EA/MCD measurements. H.H. and B.P. conducted the EA measurements. H.H. did structural characterizations (XRD). D.N. and H.H. conducted the high-field MCD measurements at the National High Magnetic Field Laboratory, with the assistance of S.M. and D.S. P.S. did the modeling and theoretical calculations: k-dependent g-factor, exciton g-factor, and MCD with ZFS. X.J. and Z.V.V. conceptualized the study and help with data analysis. X.J. wrote the first draft with input from D.N., Z.V.V. and P.S.

Acknowledgements

The authors thank Dusty Layton from the Machine Shop at the Department of Chemistry, University of Utah, who helped to upgrade the cryostat for the MCD experiment. The MCD and EA measurements at high magnetic field were supported by the Department of Energy, Office of Science, Grant DESC0014579. The MCD and EA analysis was supported by the National Science Foundation grant DMR 2054169. The high field measurements were performed at the National High Magnetic Field Laboratory in Tallahassee, FL, which is supported by National Science Foundation Cooperative Agreement No. DMR-1644779 and DMR-2128556 with the State of Florida. The preparation of the PEPI films, theoretical modeling, and data analysis were supported through the Center for Hybrid Organic-Inorganic Semiconductors for Energy (CHOISE), an Energy Frontier Research Center funded by the Office of Basic Energy Sciences, Office of Science within the US Department of Energy, grant DESC 0014579. This work was authored in part by the National Renewable Energy Laboratory (NREL), operated by Alliance for Sustainable Energy, LLC, for the U.S. Department of Energy (DOE) under Contract No. DE-AC36-08GO28308.

Funding

Department of Energy Office of Science, Grant DESC0014579 (D.N., Z.V.V.), Department of Energy Office of Science, Center for Hybrid Organic-Inorganic Semiconductors for Energy (CHOISE) grant DESC 0014579 (D.N., P.S., Z.V.V.), National Science Foundation grant DMR 2054169 (XJ).

Conflicts of Interest

The authors declare no conflicts of interest.

Data Availability Statement

The data that support the findings of this study are available from the corresponding author upon reasonable request.

References

1. C. C. Stoumpos, D. H. Cao, D. J. Clark, et al., "Ruddlesden-Popper Hybrid Lead Iodide Perovskite 2D Homologous Semiconductors," *Chemistry of Materials* 28 (2016): 2852–2867.

2. T. Ishihara, J. Takahashi, and T. Goto, "Optical Properties Due to Electronic Transitions in Two-Dimensional Semiconductors $(C_nH_{2n+1}NH_3)_2PbI_4$," *Physical Review B* 42 (1990): 11099–11107, https://doi.org/10.1103/PhysRevB.42.11099.

3. J. Calabrese, N. L. Jones, N. Harlow, D. L. Thorn, and Y. Wang, "Preparation and Characterization of Layered Lead Halide Compounds," *Journal of the American Chemical Society* 113 (1991): 2328–2330, https://doi.org/10.1021/ja00006a076.

4. K. Z. Du, Q. Tu, X. Zhang, et al., "Two-Dimensional Lead(II) Halide-Based Hybrid Perovskites Templated by Acene Alkylamines: Crystal Structures, Optical Properties, and Piezoelectricity," *Inorganic Chemistry* 56 (2017): 9291–9302, https://doi.org/10.1021/acs.inorgchem.7b01094.

5. Y. Zhai, S. Baniya, C. Zhang, et al., "Giant Rashba Splitting in 2D Organic-Inorganic Halide Perovskites Measured by Transient Spectroscopies," *Science Advances* 3 (2017): 1700704, https://doi.org/10.1126/sciadv.1700704.

6. K. R. Hansen, C. E. McClure, J. S. Colton, and L. Whittaker-Brooks, "Franz-Keldysh and Stark Effects in Two-Dimensional Metal Halide Perovskites," *PRX Energy* 1 (2022): 013001.

7. M. Dyksik, S. Wang, W. Paritmongkol, et al., "Tuning the Excitonic Properties of the 2D $(PEA)_2(MA)_{n-1}Pb_nI_{3n+1}$ Perovskite Family via

Quantum Confinement," *The Journal of Physical Chemistry Letters* 12 (2021): 1638–1643, https://doi.org/10.1021/acs.jpclett.0c03731.

8. C. Zhang, X. Jiang, P. C. Sercel, et al., "Dark Exciton in 2D Hybrid Halide Perovskite Films Revealed by Magneto-Photoluminescence at High Magnetic Field," *Advanced Optical Materials* 11 (2023): 2300436, https://doi.org/10.1002/adom.202300436.

9. K. Posmyk, M. Dyksik, A. Surrente, et al., "Fine Structure Splitting of Phonon-Assisted Excitonic Transition in $(PEA)_2PbI_4$ Two-Dimensional Perovskites," *Nanomaterials* 13 (2023): 1119, https://doi.org/10.3390/nano13061119.

10. L. Ni, U. Huynh, A. Cheminal, et al., "Real-Time Observation of Exciton–Phonon Coupling Dynamics in Self-Assembled Hybrid Perovskite Quantum Wells," *ACS Nano* 11 (2017): 10834–10843, https://doi.org/10.1021/acsnano.7b03984.

11. J.-C. Blancon, A. V. Stier, H. Tsai, et al., "Scaling Law for Excitons in 2D Perovskite Quantum Wells," *Nature Communications* 9 (2018): 2254, https://doi.org/10.1038/s41467-018-04659-x.

12. D. B. Straus and C. R. Kagan, "Photophysics of Two-Dimensional Semiconducting Organic–Inorganic Metal-Halide Perovskites," *Annual Review of Physical Chemistry* 73 (2022): 403–428, https://doi.org/10.1146/annurev-physchem-082820-015402.

13. K. Tanaka, F. Sano, T. Takahashi, T. Kondo, R. Ito, and K. Ema, "Two-Dimensional Wannier Excitons in a Layered-Perovskite-Type Crystal $(C_6H_{13}NH_3)_2PbI_4$," *Solid State Communications* 122 (2002): 249–252, https://doi.org/10.1016/S0038-1098(02)00126-6.

14. K. Tanaka, T. Takahashi, T. Kondo, T. Umebayashi, K. Asai, and K. Ema, "Image Charge Effect on Two-Dimensional Excitons in an Inorganic-Organic Quantum-Well Crystal," *Physical Review B* 71 (2005): 045312, https://doi.org/10.1103/PhysRevB.71.045312.

15. S. G. Motti, M. Kober-Czerny, M. Righetto, et al., "Exciton Formation Dynamics and Band-Like Free Charge-Carrier Transport in 2D Metal Halide Perovskite Semiconductors," *Advanced Functional Materials* 33 (2023): 2300363.

16. Y. Cho and T. C. Berkelbach, "Optical Properties of Layered Hybrid Organic–Inorganic Halide Perovskites: A Tight-Binding GW-BSE Study," *The Journal of Physical Chemistry Letters* 10 (2019): 6189–6196, https://doi.org/10.1021/acs.jpclett.9b02491.

17. D. Feldstein, R. Perea-Causín, S. Wang, et al., "Microscopic Picture of Electron–Phonon Interaction in Two-Dimensional Halide Perovskites," *The Journal of Physical Chemistry Letters* 11 (2020): 9975–9982, https://doi.org/10.1021/acs.jpclett.0c02661.

18. X. L. Yang, S. H. Guo, F. T. Chan, K. W. Wong, and W. Y. Ching, "Analytic Solution of a Two-Dimensional Hydrogen Atom. I. Nonrelativistic Theory," *Physical Review A* 43 (1991): 1186–1196, https://doi.org/10.1103/PhysRevA.43.1186.

19. K. Posmyk, M. Dyksik, A. Surrente, et al., "Exciton Fine Structure in 2D Perovskites: The out-Of-Plane Excitonic State," *Advanced Optical Materials* 12 (2023): 2300877.

20. T. Kataoka, T. Kondo, R. Ito, S. Sasaki, K. Uchida, and N. Miura, "Magneto-Optical Study on the Excitonic Spectrum of $(C_6H_{13}NH_3)_2PbI_4$," *Physica B: Condensed Matter* 184 (1993): 132–136, https://doi.org/10.1016/0921-4526(93)90336-5.

21. K. Tanaka, T. Takahashi, T. Kondo, et al., "Electronic and Excitonic Structures of Inorganic–Organic Perovskite-Type Quantum-Well Crystal $(C_4H_9NH_3)_2PbBr_4(C_4H_9NH_3)_2PbBr_4$," *Japanese Journal of Applied Physics* 44 (2005): 5923, https://doi.org/10.1143/JJAP.44.5923.

22. P. C. Sercel, "Theory of Excitons in Metal Halide Perovskites," *Hybrid Organic Inorganic Perovskites: Physical Properties and Applications*, 1st ed., edited by Z. V. Vardeny and M. Beard (World Scientific, 2022), 63–113.

23. K. Posmyk, N. Zawadzka, M. Dyksik, et al., "Quantification of Exciton Fine Structure Splitting in a Two-Dimensional Perovskite Compound," *The Journal of Physical Chemistry Letters* 13 (2022): 4463–4469, https://doi.org/10.1021/acs.jpclett.2c00942.

24. T. T. H. Do, A. G. Del Águila, D. Zhang, et al., "Bright Exciton Fine-Structure in Two-Dimensional Lead Halide Perovskites," *Nano Letters* 20 (2020): 5141–5148, https://doi.org/10.1021/acs.nanolett.0c01364.

25. P. J. Stephens, "Magnetic Circular Dichroism," *Advances in Chemical Physics*, edited by I. Prigogine and S. A. Rice (John Wiley & Sons, 1976), 197–264.

26. C. Harkort, D. Kudlacik, N. E. Kopteva, et al., "Spin-Flip Raman Scattering on Electrons and Holes in Two-Dimensional $(PEA)_2PbI_4$ Perovskites," *Small* 19 (2023): 2300988.

27. E. Kirstein, E. A. Zhukov, D. R. Yakovlev, et al., "Coherent Spin Dynamics of Electrons in Two-Dimensional $(PEA)_2PbI_4$ Perovskites," *Nano Letters* 23 (2023): 205–212.

28. Z. G. Yu, "Effective-Mass Model and Magneto-Optical Properties in Hybrid Perovskites," *Scientific Reports* 6 (2016): 28576, https://doi.org/10.1038/srep28576.

29. T. Deilmann, P. Krüger, and M. Rohlfing, "Ab Initio Studies of Exciton g Factors: Monolayer Transition Metal Dichalcogenides in Magnetic Fields," *Physical Review Letters* 124 (2020): 226402, https://doi.org/10.1103/PhysRevLett.124.226402.

30. C. Katan, N. Mercier, and J. Even, "Quantum and Dielectric Confinement Effects in Lower-Dimensional Hybrid Perovskite Semiconductors," *Chemical Reviews* 119 (2019): 3140–3192, https://doi.org/10.1021/acs.chemrev.8b00417.

31. J. V. Passarelli, C. M. Mauck, S. W. Winslow, et al., "Tunable Exciton Binding Energy in 2D Hybrid Layered Perovskites Through Donor–Acceptor Interactions Within The Organic Layer," *Nature Chemistry* 12 (2020): 672–682, https://doi.org/10.1038/s41557-020-0488-2.

32. E. Amerling, S. Baniya, E. Lafalce, C. Zhang, Z. V. Vardeny, and L. Whittaker-Brooks, "Electroabsorption Spectroscopy Studies of $(C_4H_9NH_3)_2PbI_4$ Organic–Inorganic Hybrid Perovskite Multiple Quantum Wells," *Journal of Physical Chemistry Letters* 8 (2017): 4557–4564.

33. S. Neutzner, F. Thouin, D. Cortecchia, A. Petrozza, C. Silva, and A. R. Srimath Kandada, "Exciton-Polaron Spectral Structures in Two-Dimensional Hybrid Lead-Halide Perovskites," *Physical Review Materials* 2 (2018): 064605, https://doi.org/10.1103/PhysRevMaterials.2.064605.

34. D. B. Straus, S. Hurtado Parra, N. Iotov, et al., "Direct Observation of Electron–Phonon Coupling and Slow Vibrational Relaxation in Organic–Inorganic Hybrid Perovskites," *Journal of the American Chemical Society* 138 (2016): 13798–13801, https://doi.org/10.1021/jacs.6b08175.

35. R. J. Elliott, "Intensity of Optical Absorption by Excitons," *Physical Review* 108 (1957): 1384–1389, https://doi.org/10.1103/PhysRev.108.1384.

36. R. R. Guseinov, "Coulomb Interaction and Excitons in a Superlattice," *Physica Status Solidi (b)* 125 (1984): 237–243.

37. M. Steger, S. M. Janke, P. C. Sercel, et al., "On The Optical Anisotropy in 2D Metal-Halide Perovskites," *Nanoscale* 14 (2022): 752–765.

38. N. S. Rytova, "Screened Potential of a Point Charge in a Thin Film," *Moscow University Physics Bulletin* 3 (1967): 30–37.

39. L. V. Keldysh, "Coulomb Interaction in Thin Semiconductor and Semi Metal Films," *Journal of Experimental and Theoretical Physics* 29 (1979): 716.

40. E. Hanamura, N. Nagaosa, M. Kumagai, and T. Takagahara, "Quantum Wells With Enhanced Exciton Effects and Optical Non-Linearity," *Materials Science and Engineering: B* 1 (1988): 255–258, https://doi.org/10.1016/0921-5107(88)90006-2.

41. L. M. Roth, B. Lax, and S. Zwerdling, "Theory of Optical Magneto-Absorption Effects in Semiconductors," *Physical Review* 114 (1959): 90–104, https://doi.org/10.1103/PhysRev.114.90.

42. K. Gawarecki and M. Zieliński, "Electron G-Factor in Nanostructures: Continuum media and Atomistic Approach," *Scientific Reports* 10 (2020): 22001, https://doi.org/10.1038/s41598-020-79133-0.

43. E. O. Kane, "Band Structure of Indium Antimonide," *Journal of Physics and Chemistry of Solids* 1 (1957): 249–261, https://doi.org/10.1016/0022-3697(57)90013-6.

44. Y. Nagamune, S. Takeyama, and N. Miura, "Exciton Spectra and Anisotropic Zeeman Effect in PbI_2 at High Magnetic Fields up to 40 T," *Physical Review B* 43 (1991): 12401–12405, https://doi.org/10.1103/PhysRevB.43.12401.

45. S. R. Meliakov, E. A. Zhukov, V. V. Belykh, et al., "Landé G - Factors of Electrons and Holes Strongly Confined in $CsPbI_3$ Perovskite Nanocrystals in Glass," *Nanoscale* 17 (2025): 6522–6529, https://doi.org/10.1039/D4NR04602A.

46. E. Kirstein, D. R. Yakovlev, M. M. Glazov, et al., "The Landé Factors of Electrons and Holes in Lead Halide Perovskites: Universal Dependence on the Band Gap," *Nature Communications* 13 (2022): 3062, https://doi.org/10.1038/s41467-022-30701-0.

47. S.-Y. Chen, Z. Lu, T. Goldstein, et al., "Luminescent Emission of Excited Rydberg Excitons From Monolayer WSe_2," *Nano Letters* 19 (2019): 2464–2471, https://doi.org/10.1021/acs.nanolett.9b00029.

48. K. Posmyk, N. Zawadzka, Lucja Kipczak, et al., "Bright Excitonic Fine Structure in Metal-Halide Perovskites: From Two-Dimensional to Bulk," *Journal of the American Chemical Society* 146 (2024): 4687–4694, https://doi.org/10.1021/jacs.3c11957.

49. A. Miyata, A. Mitioglu, P. Plochocka, et al., "Direct measurement of the exciton binding energy and effective masses for charge carriers in organic–inorganic tri-Halide perovskites," *Nature Physics* 11 (2015): 582–587, https://doi.org/10.1038/nphys3357.

50. M. Dyksik, "Using the Diamagnetic Coefficients to Estimate the Reduced Effective Mass in 2D Layered Perovskites: New Insight From High Magnetic Field Spectroscopy," *International Journal of Molecular Sciences* 23 (2022): 12531, https://doi.org/10.3390/ijms232012531.

51. D. E. Aspens, "Modulation Spectroscopy/Electric Field Effects on the Dielectric Function of Semiconductors," *Handbook on Semiconductors, Optical Properties of Solids*, edited by T. S. Moss and M. Balkanski (North-Holland Publishing Company, 1980), 109–154.

Supporting Information

Additional supporting information can be found online in the Supporting Information section.

Supporting File: adfm74939-sup-0001-SuppMat.docx.